

# Highly directionally spread, overturning breaking waves modelled with Smoothed Particle Hydrodynamics: a case study involving the Draupner wave.

T. Kanehira<sup>a</sup>, M. L. McAllister<sup>\*b</sup>, S. Draycott<sup>c</sup>, T. Nakashima<sup>a</sup>, N. Taniguchi<sup>a</sup>, D. M. Ingram<sup>d</sup>, T. S. van den Bremer<sup>e,b</sup>, H. Mutsuda<sup>a</sup>

<sup>a</sup>*Graduate School of Advanced Science and Engineering, Hiroshima University, Higashi-Hiroshima, Japan*

<sup>b</sup>*Department of Engineering Science, University of Oxford, Oxford, UK*

<sup>c</sup>*Department of Mechanical, Aerospace and Civil Engineering, University of Manchester, Manchester, UK*

<sup>d</sup>*School of Engineering, The University of Edinburgh, Edinburgh, UK*

<sup>e</sup>*Faculty of Civil Engineering and Geosciences, Delft University of Technology, Delft, The Netherlands*

---

## Abstract

Wave breaking in the ocean affects the height of extreme waves, energy dissipation, and interaction between the atmosphere and upper ocean. Numerical modelling is a critical step in understanding the physics of wave breaking and offers insight that is hard to gain from field data or experiments. High-fidelity numerical modelling of three-dimensional breaking waves is extremely challenging. Conventional grid-based numerical methods struggle to model the steep and double-valued free surfaces that occur during wave breaking. The Smoothed Particle Hydrodynamics (SPH) method does not fall prey to these issues. Herein, we examine the SPH method's ability to model highly directionally spread overturning breaking waves by numerically reproducing the experiments presented in McAllister et al. [*J. Fluid Mech.* Vol. 860, 2019, pp. 767–786]. We find that the SPH method reproduces the experimental observations well; when comparing experimental and numerical measurements we achieve coefficient of determination values of 0.92 – 0.95, with some smaller-scale features less well reproduced owing to finite resolution. We also examine aspects of the simulated wave's geometry and kinematics and find that existing breaking criteria are difficult to apply in highly directionally spread conditions.

**Keywords:** Wave breaking, Smoothed Particle Hydrodynamics, Directional spreading, Freak waves

---

## 1. Introduction

Unexpectedly large, extreme or ‘freak’ waves are enigmatic oceanic phenomena that have attracted a large amount of scientific and popular attention. Studies have shown such waves to exist [1, 2, 3], shifting their existence from the realm of folklore to reality. Several shipping catastrophes and accidents are thought to have been caused by freak waves [4, 5, 6, 7, 8, 9]. As a result, much work has focused upon understanding why these waves occur and evaluating the risk they pose (see [10, 11, 12] for reviews). Freak waves are also known to occur in other fields, such as optics [13]. While a simple single explanation why freak waves may occur does not exist [10, 11, 12], wave breaking is the process that limits wave height and is hence critical to their formation.

*In-situ* observations of freak waves provide necessary evidence of their existence [1, 2, 3]. However, such observations are often limited to isolated measurements of surface elevation and provide limited insight into the properties of and mechanisms giving rise to these freak waves. Numerical and experimental approaches can offer the opportunity to study freak waves in more detail than using in-situ observations alone. For example, in [14, 15] random simulations are carried out using the Higher-Order Spectral Method (HOSM), with inputs based on the extreme waves observed in [1, 2, 3], to examine the importance of third-order nonlinearity in creating extreme waves.

In the laboratory, it is possible to reproduce high-fidelity hydrodynamic conditions through appropriate scaling, but it can be more challenging to measure certain physical quantities, such as pressure and velocity, than others, such as surface elevation (e.g., [16]). Numerical models offer the potential to recreate extreme waves, while providing the ability to calculate readily and with high spatial resolution physical quantities that are difficult to measure in the laboratory. However, high-fidelity numerical modeling of extreme ocean waves is challenging. Surface gravity waves exist on the interface between air and water. This potentially highly nonlinear moving free surface constitutes one of the main challenges associated with numerical modelling of water waves. For more conventional grid-based potential-flow methods, this challenge may be

---

\*Corresponding author

Email address: Mark.McAllister@eng.ox.ac.uk (M. L. McAllister\*)

overcome using approaches such as deforming grids. However, grid-based methods can struggle when surface deformations become very steep or double valued, both of which occur when waves break. Eulerian multi-phase numerical models which use surface following methods such as volume-of-fluid (see [17] for a review of methods) have been implemented successfully to perform high-fidelity simulations of overturning breaking waves [18, 19]. The computational demand of such models is large and thus can necessitate small computational domains or two-dimensional simulations in many scenarios [19]. Particle-based methods such as SPH (see also [20], for an example of the Lattice Boltzmann method) do not require special treatment of the free surface, such as adaptive meshing. Moreover, moving boundaries, such as wave makers, may be readily implemented using dynamic boundary particles. Thus SPH provides an ideal way to model a full numerical wave tank, including wave generation, evolution, and breaking. An additional benefit is that SPH is globally conservative (mass and momentum), which is not the case for volume of fluid approaches [21].

SPH is making rapid advances in scientific computation, offering major advantages to those modelling multi-phase and free surface flows. Significant progress has been made since Monaghan [22] first extended the weakly-compressible form of SPH to free surface flows. This approach initially suffered from noisy pressure fields and numerical instability, yet recent advances have improved this significantly. Density-diffusion schemes have been employed to smooth the pressure fields [23, 24], and particle-shifting techniques have been successfully implemented to avoid particle clustering and numerical instability [25]. The incompressible form of SPH has also seen significant progress [26], providing improved pressure fields, yet at significantly greater computational expense. Weakly-compressible SPH has been used to simulate surface waves for a wide range of applications [27, 28, 29, 30], including deep and shallow-water conditions [31] and the study of wave breaking [32, 33]. The vast majority of published breaking wave studies that use SPH focus on uni-directional waves [34, 35], and breaking typically occurs in shallow water [32, 33]. Here, we use weakly-compressible SPH to simulate freak, breaking waves occurring in directionally spread and crossing wave systems in intermediate water depth. We use the resulting validated simulations to explore the complex nature of these events.

The Draupner wave was one of the first unexpectedly large or ‘freak’ waves to be measured [1].

It was observed in the North Sea on the 1st of January 1995, initiating a body of research aiming to understand the nature of freak waves. In a recent experimental study [36] (MC19 hereafter), this wave was reproduced in the laboratory. In addition to being the first to fully reproduce this wave at scale, providing insight into how this wave may have been created, these experimental observations raised questions about the onset of wave breaking in crossing conditions. In Kanehira et al. [37], an SPH model of the physical wave tank used in MC19 was developed, thus making it possible to replicate the experiments of MC19 numerically as a case study. We carry out this case study, firstly, to provide a means of validation and as an illustration of the capabilities of SPH for modelling of highly directionally spread overturning breaking waves; and, secondly, to enhance our understanding of the wave breaking phenomena observed.

Of the effects associated with breaking, we aim to investigate the onset of breaking and how this may affect extreme wave height. Thresholds based on wave steepness and other geometric criteria are commonly used to predict when waves will break. While simple, geometric criteria overlook much of the natural variability of surface waves and are inaccurate [38]. Kinematic and dynamic breaking criteria [39, 40] use fluid properties (e.g., velocity and acceleration), which means they can be used to detect the onset of wave breaking but are less suitable for predictive use. These criteria have been shown to detect the onset of breaking robustly for following-sea conditions over a range of water depths [40, 41, 42, 43]. We examine their application to highly directionally spread breaking waves here. Both linear and non-linear (i.e., modulational instability) focussing mechanisms can play a role in directionally spread seas (e.g., [44]), although we do not focus on identifying the type of focussing mechanism herein

The paper is laid out as follows. The numerical method and governing equations used are explained in §2. In §3, we present the results of our simulations, including a discussion on model validation (§3.1), wave geometry (§3.2), kinematics (§3.3), and breaking behaviour (§3.4). Finally, in §4, we draw conclusions.

## 2. Numerical Method

We use an SPH model of the FloWave Ocean Energy Research Facility built using Dual-SPHysics [45], which has been validated for directionally spread waves of moderate steepness

[46]. We review the numerical approach used in the following section.

## 2.1. SPH Implementation

SPH offers a Lagrangian mesh-free, particle-based method, by which continuum fluid flow can be modelled as discrete calculation points called particles that move in conjunction with fluid motion. As initially proposed by [47], physical quantities such as pressure, density and velocity can be described for each particle by spatial interpolation between neighbouring particles. The fundamental principle of the SPH method is to approximate a physical quantity  $\phi$  as follows:

$$\phi(\mathbf{r}) = \int_{\Omega} \phi(\mathbf{r}') W(\mathbf{r} - \mathbf{r}', h) d\mathbf{r}', \quad (1)$$

where  $W$  is the smoothing kernel function,  $h$  is the smoothing length,  $\mathbf{r}$  is the so-called focused position vector and  $\mathbf{r}'$  is the neighbouring position vector. Particles in the reference area  $\Omega$  contribute to the estimate of  $\phi(\mathbf{r})$ . A normalisation condition ensures that  $\int_{\Omega} W(\mathbf{r} - \mathbf{r}', h) d\mathbf{r}' = 1$ , and, as  $h$  approaches zero,  $W$  must approach the Dirac delta function ( $\delta$ ):  $\lim_{h \rightarrow 0} W(\mathbf{r} - \mathbf{r}', h) = \delta(\mathbf{r} - \mathbf{r}')$ . In this work, we utilise the quintic Wendland kernel [48],

$$W(r, h) = \alpha_D \left(1 - \frac{q}{2}\right)^4 (2q + 1), \quad 0 \leq q \leq 2, \quad (2)$$

where  $q = r/h$  is given by the distance between any two selected particles  $r$  divided by the smoothing length  $h$ , and  $\alpha_D$  is equal to  $7/(4\pi h^2)$  in 2D, and  $21/(16\pi h^3)$  in 3D. Equation (1) can be converted into discrete form (e.g., [33]):

$$\phi(\mathbf{r}_a) = \sum_{b=1}^N \phi(\mathbf{r}_b) W(\mathbf{r}_b - \mathbf{r}_a, h) V_b, \quad (3)$$

where properties for particle  $a$  are calculated as a function of all  $N$  neighbours,  $V_b$  is the volume of neighbouring particle  $b$  (noting that  $V_b = m_b/\rho_b$ ), and  $m_b$  and  $\rho_b$  represent the mass and density of particle  $b$ , respectively.

### 2.1.1. Governing equations

If we have an incompressible fluid, it may be described by continuity and the conservation of momentum:

$$\frac{D\rho}{Dt} + \rho \nabla \cdot \mathbf{u} = 0, \quad (4)$$

$$\frac{D\mathbf{u}}{Dt} = -\frac{1}{\rho}\nabla p + \mathbf{g} + \nu_0\nabla^2\mathbf{u} + \frac{1}{\rho}\nabla \cdot \vec{\tau}, \quad (5)$$

where  $D/Dt$  denotes the material derivative,  $\rho$  is the fluid density,  $\mathbf{u} = (u, v, w)$  is the velocity vector with components in the  $(x, y, z)$ -directions with  $z$  measured vertically,  $\mathbf{g}$  is gravitational acceleration,  $p$  is pressure,  $\nu_0$  is the laminar kinematic viscosity, and  $\vec{\tau}$  is the Sub-Particle Scale (SPS) stress tensor. Using the SPH approach in accordance with [33], (4) and (5) may be represented as

$$\frac{d\rho_a}{dt} = \sum_b m_b (\mathbf{u}_a - \mathbf{u}_b) \cdot \nabla_a W_{ab} + \mathcal{D}_a, \quad (6)$$

$$\begin{aligned} \frac{d\mathbf{u}_a}{dt} = & - \sum_b m_b \left( \frac{p_b}{\rho_b^2} + \frac{p_a}{\rho_a^2} \right) \nabla_a W_{ab} + \mathbf{g} \\ & + \sum_b m_b \left( \frac{4\nu_0 r_{ab} \cdot \nabla_a W_{ab}}{(\rho_a + \rho_b)(r_{ab}^2 + \zeta^2)} \right) (\mathbf{u}_a - \mathbf{u}_b) \\ & + \sum_b m_b \left( \frac{\vec{\tau}^b}{\rho_b^2} + \frac{\vec{\tau}^a}{\rho_a^2} \right) \cdot \nabla_a W_{ab}, \end{aligned} \quad (7)$$

where  $\zeta^2 = 0.01h^2$ ,  $r_{ab} = r_a - r_b$ ,  $r_{ab} = |r_{ab}|$ , and  $\nabla_a W_{ab}$  is the derivative of the smoothing kernel with respect to the coordinates of particle  $a$ . The symbol  $\mathcal{D}_a$  in (6) represents the diffusive term used in the delta-SPH scheme [23]. The delta-SPH coefficient used here is 0.1. In this study, the above technique is used to reduce the high-frequency density fluctuations (caused by natural particle disorder), which can introduce significant noise in the pressure fields due to the stiff equation of state (see (8)). In (7), the third right-hand-side term represents the laminar viscosity presented in [49], and the fourth term is the Sub-Particle Scale (SPS) turbulence model first introduced by [50] and formulated in Weakly Compressible SPH in [33]. We use the Smagorinsky constant (0.12) following [33].

For a weakly compressible fluid, pressure can be computed using an explicit numerical algorithm. Here, rather than solving Poisson's equation (an implicit method), to reduce computational cost, an equation of state that relates pressure to density is used:

$$p = b \left[ \left( \frac{\rho}{\rho_0} \right)^\gamma - 1 \right]. \quad (8)$$

where  $\gamma = 7$ ,  $b = c_0^2 \rho_0 / \gamma$ ,  $\rho_0 = 1000 \text{ kg/m}^3$  is the reference density, and  $c_0$  is the speed of sound.

Equation (8) represent a stiff equation of state, with small changes in density causing large pressure fluctuations.

A symplectic second-order time-integration method is applied using corrector and predictor stages. As in [51], a variable time step  $\Delta t$  is utilised in this study.

### 2.1.2. Boundary conditions and tank geometry

Fig. 1 shows the geometry of the FloWave tank [52] recreated numerically in [37] and to be used in this paper. The tank has a diameter  $D = 25$  m and is 2 m deep. Waves are generated and absorbed by the 168 individually-controlled hinged flap-type wavemakers that form the circumference of the tank. These wavemakers constitute the radial boundary condition of our numerical domain. Accordingly, the wavemakers are modelled as Dynamic Boundary Particles (DBPs) using the Dynamic Boundary Condition (DBC) developed by [53]. The tank floor is also modelled using stationary DBPs. The real tank has gratings for current circulation located on the tank floor at the bottom of the wavemakers that do not feature in the numerical model, which has a flat bottom. The angle of rotation (in the vertical, radial plane)  $\Phi_p(t)$  of each of the 168 wave paddles was recorded during each of the experiments in MC19. These values are used to force the position of the DBPs that form the wavemakers, exactly as in the experiment.

### 2.2. Experimental Conditions from MC19

In MC19, the time series measured at the Draupner platform by [1] was decomposed into two wave systems, which cross each other (a main and a transverse wave system; see MC19 for details). This decomposition was based on previous work [54], which showed certain aspects of the measured wave's nonlinear structure could not be reproduced under so-called following-sea (non-crossing) conditions. Experiments in MC19 were carried out for three scenarios, setting the angle between the two systems  $\Delta\theta$  to  $0^\circ$  (following-sea conditions, i.e. no crossing),  $60^\circ$ , and  $120^\circ$ . Both wave systems are directionally spread about their respective mean directions with a wrapped normal spreading function of width  $30^\circ$  applied to the amplitude distribution. Here, we carry out simulations of the same three experiments. The directions of propagation of both the main and transverse wave systems (or groups) are shown as the blue (main) arrow and the red (transverse)

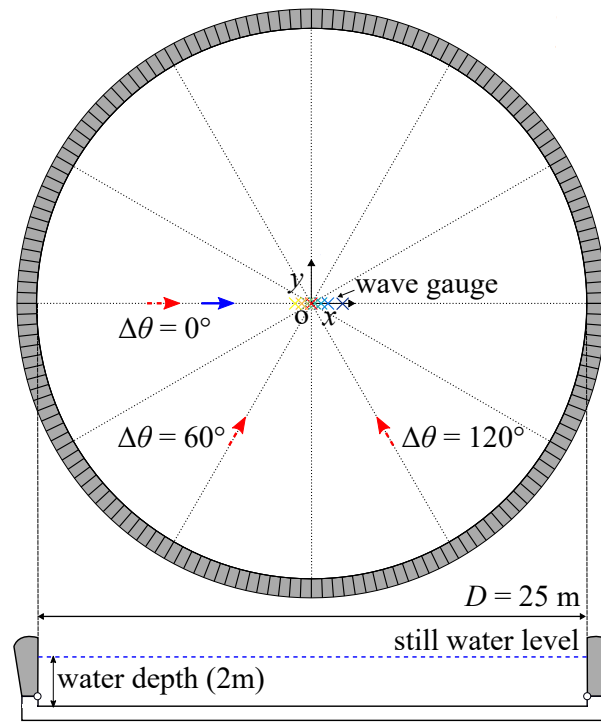


**Fig. 1** Schematic diagram of the experimental and numerical wave tank with eight wave gauges (coloured crosses) installed along the  $x$ -axis near the centre of the tank. The blue arrow shows the main wave group's direction, and the red dashed arrows mark the three different transverse wave groups' directions for the three simulations.

160 dashed arrows in Fig. 1. In all three simulations, the main wave system propagated along the  $x$ -  
161 axis, from left to right, whereas the transverse waves propagated from the three different directions.  
162 In MC19, the target surface elevation at the centre of the tank ( $x = 0, y = 0$ ) was generated  
163 iteratively by adjusting the phase and amplitude of the decomposed time series. The wavemaker  
164 motions recorded for these experiments are used to generate the waves in our simulations.

165 In MC19, an array of eight resistance-type wave gauges were installed along the  $x$ -axis at the  
166 positions listed in Tab. 1 (see Fig. 1). We use the measurements made at these eight gauges for  
167 model validation herein. All results will be presented at laboratory scale.

**Table 1** Position of the wave gauges.

WG	1	2	3	4	5	6	7	8
$x$ (m)	-0.5	-0.3	-0.1	0	0.1	0.3	0.5	1
$y$ (m)	0	0	0	0	0	0	0	0

### 168 2.3. Numerical Set-up and Conditions

169 The parameters of the numerical simulations carried out in this study are shown in Tab. 2.  
170 To ensure numerical convergence, we have run 12 cases in total. We have reduced the particle  
171 spacing  $d_p$ , which is related to the smoothing length  $h$  by  $h = c_h \sqrt{3d_p^2}$  with  $c_h$  the smoothing  
172 length coefficient, in four refinements from 0.1 m to 0.02 m, for each of the three experiments  
173 carried out in MC19 that we aim to reproduce numerically. We non-dimensionalise the maximum  
174 wave height measured in all experiments ( $H_D = 0.73$  m) by particle spacing ( $d_p$ ), thus providing  
175 the representative number of particles from crest to trough  $H_D/d_p$ .

176 The total number of particles ( $N_p$ ) was between 1.12 and 127 million, and the run time for  
177 the finest particle cases was approximately 167 hrs using a GPU (NVIDIA, Quadro RTX 8000).  
178 We adopted a smoothing length coefficient  $c_h = 1.0$ . This value is smaller than the recommended  
179 values of between 1.2 and 1.5 for wave propagation in DualSPHysics; setting  $c_h = 1.0$  achieved  
180 better results with reduced run time. This could be related to the particle resolution used in this  
181 study. The particle spacing used was relatively large owing to the large simulation domain (982

182  $\text{m}^3$ ) and computational constraints on the total number of particles ( $N_p$ ). Note that the value of  
 183  $c_h = 1.0$  results in a ratio of  $h/d_p = 1.73$ , and this ratio is close to the value of 1.7 used in [55].

**Table 2** Numerical conditions for the three different simulations for four different particle spacings.

Case	$\Delta\theta$	$d_p/D (\times 10^{-3})$	$H_D/d_p$	$N_p (\times 10^6)$
1, 2, 3, 4	$0^\circ$	4.0, 2.0, 1.2, 0.8	7, 15, 24, 37	1.12, 8.61, 38.6, 127
5, 6, 7, 8	$60^\circ$	”	”	”
9, 10, 11, 12	$120^\circ$	”	”	”

#### 184 2.4. Convergence

185 We evaluate the model’s convergence using the coefficient of the determination ( $r^2$ ). This value  
 186 is used to quantify how well the modelled results match the experimental data. Fig. 2a shows  $r^2$   
 187 values achieved for the three experiments as a function the representative number of particles  
 188 from crest to trough  $H_D/d_p$ . In all three cases, the  $r^2$  values increase monotonically and converge  
 189 as particle spacing is reduced, reaching approximately 0.95. Implementing a finer particle spacing  
 190 may improve the reproduction, but the improvement will be diminishing and is outwith the scope  
 191 of this study owing to computational constraints. The value of  $r^2$  is calculated using the measured  
 192 surface elevation over the duration of our simulations and physical experiments. Using  $r^2$  in this  
 193 way (as a measure of convergence) may obscure how well our model produces finer-scale details  
 194 of fluid flow (Fig. 2b-d); we return to this in §3.1.

### 195 3. Results

196 To examine the results of our simulations, we first compare our simulations to observations  
 197 made in MC19 as a means of model validation in §3.1. We then use the additional available  
 198 information gained from our numerical simulations to examine aspects of the extreme wave’s  
 199 geometry (§3.2), kinematics (§3.3), and breaking behaviour (§3.4). The numerical results we  
 200 present in this section correspond to the finest resolution simulations that were carried out (cases  
 201 4, 8, and 12).

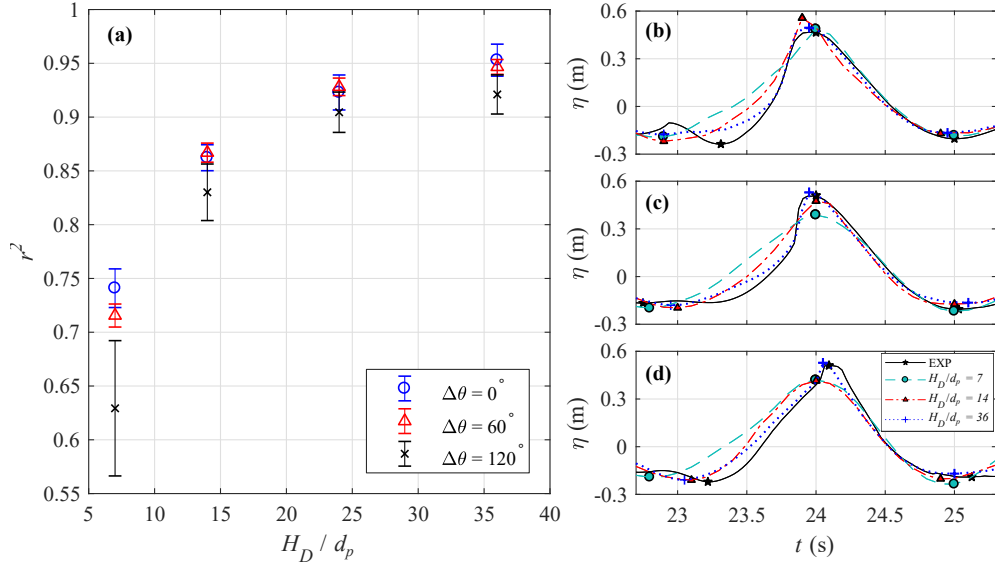


**Fig. 2** Convergence as a function of particle spacing, evaluated using the coefficient of determination  $r^2$  for the three different crossing angles  $\Delta\theta = 0, 60, 120^\circ$ , values of  $r^2$  are averaged over the eight wave gauges with error bars showing the corresponding standard deviation. In panel a, the horizontal axis represents the number of particles from crest to trough  $H_D/d_p$ , where  $H_D = 0.73$  m is the maximum wave height of the measurements and  $d_p$  is the initial particle spacing. Panels b, c and d represent comparison of our modelled reproduction and the experimental reproduction (MC19) of the Draupner wave for the three crossing angles  $\Delta\theta = 0^\circ$  (b),  $60^\circ$  (c),  $120^\circ$  (d). The markers indicate the maximum and minimum points of the surface elevation.

### 3.1. Experimental Validation

In Fig. 3, we compare time series of free surface elevation extracted from our simulations to those measured during the experiments; measurements from wave gauges 1 to 7 are shown from bottom to top. As also reflected by the high  $r^2$  values in Fig. 2, the simulated surface elevations agree well with the experimental measurements. At the time of the extreme wave crest, there are some differences between small-scale features of the surface elevation, which may be a result of finite particle spacing in our simulations or experimental error. For  $\Delta\theta = 120^\circ$ , the simulations appear to capture the sharp variations of the surface elevation after breaking, as illustrated in the inset plot (panel c). In all three cases, the post-breaking measurements (gauges 5 and higher) are well reproduced.

Tab. 3 compares wave heights and crest amplitudes observed during the experiments (MC19) and numerical simulations (SPH). The numerical and experimental values agree closely and follow the same general trend, increasing with crossing angle. The difference between numerical and experimental wave heights is 1-4% and corresponds to small-scale features of the surface elevation.

**Table 3** Wave heights from zero-down-crossing  $H_d$  and zero-up-crossing  $H_u$  and crest amplitudes  $a$  measured in the experiments (MC19), simulations (SPH) and in the field (Draupner). The values are calculated using time series measured at the centre of the tank ( $x = 0, y = 0$ ).

$2[1]*\Delta\theta$	$H_d$ (m)		$H_u$ (m)		$a$ (m)	
	MC19	SPH	MC19	SPH	MC19	SPH
$0^\circ$	0.69	0.67	0.67	0.66	0.47	0.50
$60^\circ$	0.68	0.71	0.68	0.69	0.51	0.53
$120^\circ$	0.73	0.74	0.70	0.70	0.51	0.53
Draupner	0.71		0.73		0.53	

In Fig. 4, we draw qualitative comparison between experimental and numerical observations; the top row shows a series of still images capture during the three different experiments using a camera positioned at the edge of the wave tank, the bottom row shows corresponding rendered images produced using the numerical simulations. Each column corresponds to an individual ex-

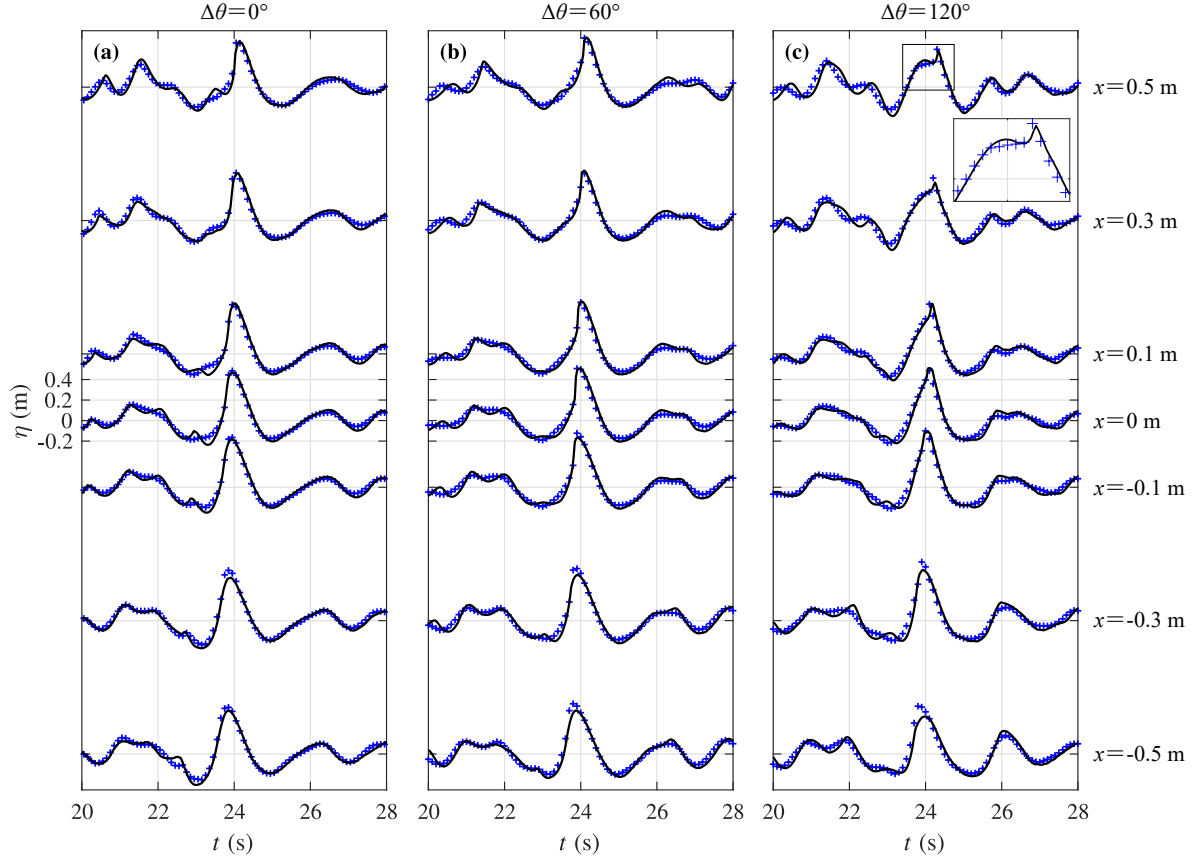


**Fig. 3** Free surface elevation measured in our simulations (blue markers) and MC19 (black lines) at gauge locations positioned along the  $x$ -axis (see Tab. 1) for  $\Delta\theta = 0^\circ$  (a),  $60^\circ$  (b), and  $120^\circ$  (c). The gauge number increases from the bottom to the top of the figure.

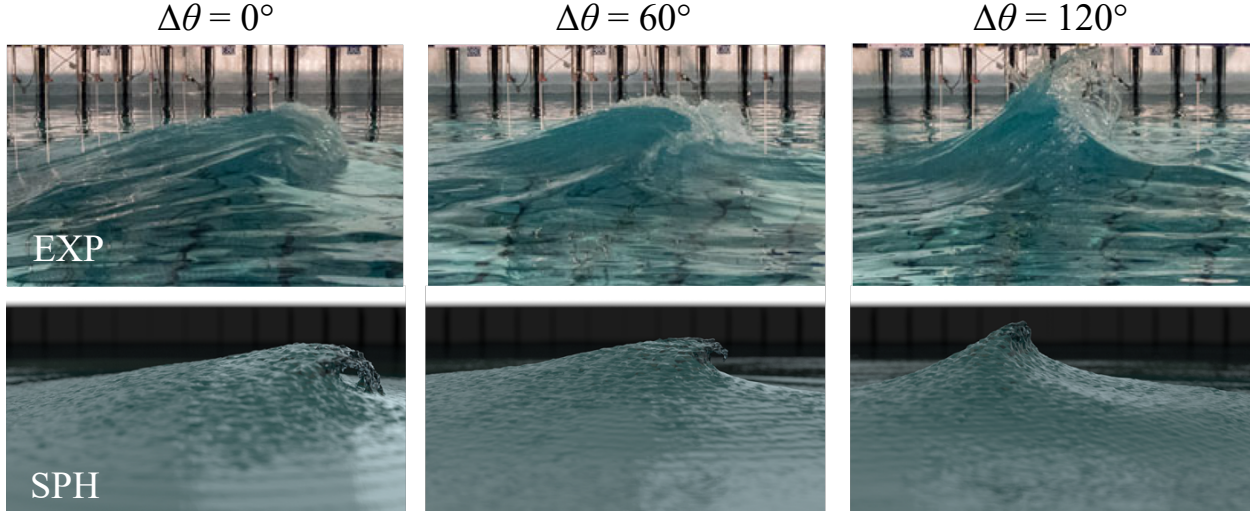


**Fig. 4** Images of free surface elevation captured using a camera in MC19 (top row, EXP) and rendered using the results of our SPH simulations (bottom row, SPH) for  $\Delta\theta = 0^\circ$  (left),  $60^\circ$  (middle), and  $120^\circ$  (right).

periment carried out for a different crossing angle  $\Delta\theta$ . In each image, the main wave direction ( $x$ -axis) is from left to right. MC19 showed that the transition from plunging breaking to upward-jet formation shown in Fig. 4 was critical to reconstructing the Draupner wave measured in the field, with plunging breaking apparently limiting the achievable crest height more significantly than upward-jet formation. This transition is also observed in the numerical simulations; as the angle  $\Delta\theta$  is increased, crest overturning reduces. Both series of images depict qualitatively similar behaviour. Finer details, such as spray formation, are not captured, as is clearest in the two right-hand panels of Fig. 4. The small differences between measurements (MC19) and simulations (SPH) in Fig. 4 are most likely caused by the finite particle spacing used. When implementing the SPH method, continuum quantities of the fluid domain are smoothed by (1), and so the reproduction of features finer than the particle spacing is not possible. To improve these results, a global particle resolution finer than these features, or a multi-resolution technique could be applied. Based on these observations, we argue that the current simulations may be used to gain additional insight into the larger-scale aspects of the waves geometry and kinematics, with less emphasis on small-scale features, such as spray and droplet formation.

### 3.2. Wave Geometry

Wave geometry is often used to predict the onset of wave breaking and has broader implications for the loading of offshore structures and bodies and the probability of encountering extreme waves. The majority of wave measurement devices, deployed offshore or used in laboratories, provide time-series measurements of surface elevation and hence do not directly measure wave geometry. To infer wave geometry from time-domain measurements, it is common to use the linear dispersion relation  $\omega^2 = gk \tanh(kh)$ , where  $\omega$  is the angular frequency,  $k$  the wavenumber,  $h$  the water depth, and  $g$  the acceleration due to gravity. When waves become steep, the role of nonlinearity increases, which can affect dispersion. Hence, estimating wave geometry from time-series measurements in this manner can result in errors [56]. When waves propagate in many different directions, this also affects their geometry. Thus, the spectral bandwidth of waves in both frequency and direction affects the accuracy of this method of approximating wave geometry from time-domain measurements using the linear dispersion relation [56, 57]. In the following section, we measure the actual (spatial) geometry of the waves in our simulations and compute geometric parameters to describe this. We then compare the measured values of these geometric parameters to values approximated using time-series measurements and linear dispersion.

#### 3.2.1. Geometric definitions

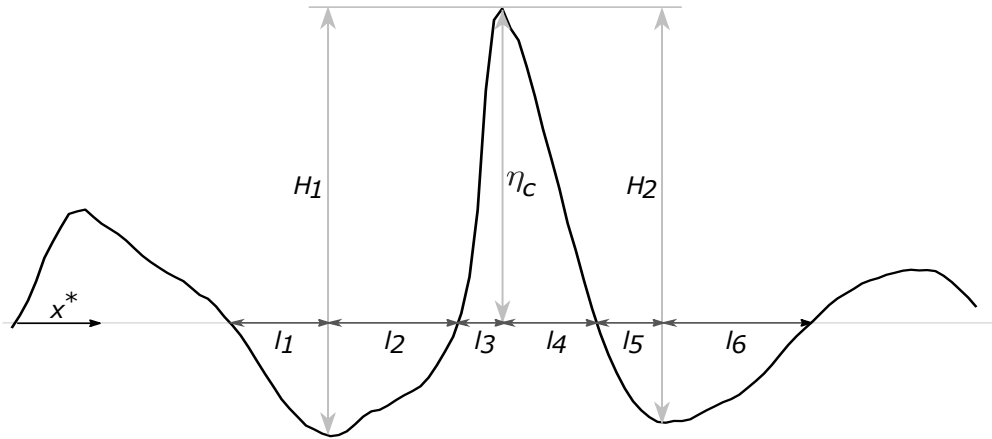


**Fig. 5** Diagram showing definitions for geometric parameters.

Fig. 5 defines the parameters we use to assess wave geometry. The following definitions are

used for comparison between the time-domain approximations and spatial measurements. The representative wave height  $H^*$  is defined as:

$$H^* = \frac{H_1 + H_2}{2}. \quad (9)$$

Time-domain equivalents are calculated based on the maxima and minima of the time-domain surface elevation measurements (up and down-crossing wave heights are denoted by  $H_{1t}$  and  $H_{2t}$ , and the representative time-domain wave height is denoted by  $H_t^*$ ).

Analogously to the representative wave height, the representative wavelength  $L^*$  is defined as:

$$L^* = \frac{L_1 + L_2}{2}, \quad (10)$$

where  $L_1 = l_1 + l_2 + l_3 + l_4$  and  $L_2 = l_3 + l_4 + l_5 + l_6$ . For time-domain equivalents, the up-crossing ( $T_{1t} = t_1 + t_2 + t_3 + t_4$ ) and down-crossing periods ( $T_{2t} = t_3 + t_4 + t_5 + t_6$ ) are used in combination with the linear dispersion relation to obtain  $L_{1t}$  and  $L_{2t}$  and hence  $L_t^*$ . Note that  $k = 2\pi/L$  and  $\omega = 2\pi/T$ . A representative steepness, equivalent to  $ka$  (i.e., the product of wavenumber  $k$  and surface elevation amplitude  $a$ ), can be defined as  $2\pi\eta_c/L^*$ , or  $2\pi\eta_c/L_t^*$  in the case of time-domain measurements. We also calculate,

$$\varphi_s = \arctan\left(\frac{\eta_c}{l_4}\right), \quad (11)$$

as a measure of the crest-front steepness, because this is suggested as a robust parameter for predicting the onset of wave breaking in [43].

To measure the spatial properties shown in Fig. 5, it is necessary to choose a direction of propagation over which characteristic wavelengths may be defined. For scenarios where the waves travel in a single mean direction (i.e., following seas), this is trivial. In more complex crossing conditions, a characteristic wave direction must be approximated. To do so, we define a coordinate system  $(x^*, y^*)$  that is obtained by rotating the coordinate system  $(x, y)$  clockwise by an angle  $\theta$ . The coordinate  $x^*$  is referred to as the ‘observation direction’. Spatial measurements presented below are taken in the instantaneous crest direction  $\theta = \theta^*$  (see §3.4 for a precise definition). The instantaneous crest directions we obtain are  $\theta^* = 0^\circ, 35^\circ$ , and  $50^\circ$  for  $\Delta\theta = 0^\circ, 60^\circ$ , and  $120^\circ$ , respectively.

### 3.2.2. Geometry of simulated waves

The measured wave geometry parameters and those estimated from time-domain measurements are presented in Tab. 4. Spatial measurements are calculated at  $t_{\text{focus}}$ , which is the time when the maximum value of the crest elevation  $\eta_c$  is recorded at  $(x, y) = (0, 0)$  (so that  $\eta_c$  and  $\eta_{ct}$  are equal by definition). The corresponding surface elevations in different observation directions  $\theta$ , are shown in Fig. 6 along with the wavelength  $L_2$  as a function of  $\theta$  at  $t_{\text{focus}}$  (middle column), and the local surface gradient (right column). Fig. 3 shows the measurements at  $(x, y) = (0, 0)$  used to estimate wave geometry in the time domain.

**Table 4** Geometric parameters calculated from spatial measurements and estimated from time-domain measurements.

$\Delta\theta$ [°]	$\eta_c$ [m]	$H_2$ [m]	$H_1$ [m]	$H^*$ [m]	$L_2$ [m]	$L_1$ [m]	$L^*$ [m]	$2\pi\eta_c/L^*$	$\varphi_s$ [°]
0	0.521	0.653	0.644	0.649	8.20	10.36	9.28	0.353	21.3
60	0.541	0.573	0.576	0.575	10.1	12.3	11.2	0.304	8.25
120	0.562	0.617	0.631	0.624	8.66	11.7	10.2	0.347	16.8
$\Delta\theta$ [°]	$\eta_c$ [m]	$H_{2t}$ [m]	$H_{1t}$ [m]	$H_t^*$ [m]	$L_{2t}$ [m]	$L_{1t}$ [m]	$L_t^*$ [m]	$2\pi\eta_c/L_t^*$	
0	0.521	0.672	0.662	0.667	7.33	6.97	7.15	0.458	
60	0.541	0.714	0.698	0.706	7.49	7.14	7.31	0.464	
120	0.562	0.746	0.707	0.726	6.84	6.83	6.83	0.517	

The information contained in Tab. 4, along with Fig. 3 and Figs. 6a, d, and g, illustrate a number of differences between spatial and temporal measurements. First, the wave heights obtained from time-domain measurements are larger than those calculated from spatial measurements for all crossing angles. This is a result of the dispersive focusing that occurs because of the broad-banded nature of the waves. Second, it is clear that wavelengths estimated from time-domain measurements are significantly smaller than the wavelengths obtained from spatial measurements. The relative error in the time-domain wavelength estimation for the following-sea case ( $\Delta\theta = 0^\circ$ ), for which the characteristic wavelength is a well-defined property, is 23% (based on  $L^*$  values). For this moderately spread case, this error arises as a result of both bandwidth and nonlinearity (see

also [57], where values of 20-30 % are reported and a detailed discussion of effects of bandwidth and nonlinearity is provided). For large crossing angles, wavelength becomes less well-defined.

Large horizontal asymmetry is evident from  $L_1$  values that are larger than  $L_2$  for all crossing angles in Tab. 4. In contrast, estimates of wavelength from the time domain do not display the same asymmetry and are approximately the same for all crossing angles. The increased directional bandwidth for these cases increases the discrepancy between temporally estimated and spatially measured wavelengths. This results in large discrepancies in apparent wave steepness. If only time-domain measurements are available, the steepness can be over-estimated by over 50% (53% for  $\Delta\theta = 60^\circ$  and 49% for  $\Delta\theta = 120^\circ$ ). If the steepness parameters were based on the characteristic wave height instead of the crest amplitude, the over-estimation would be as large as 88% for  $\Delta\theta = 60^\circ$ . These spatial steepness values may not, however, be particularly representative of the local wave geometry due to the unusual wave profiles recorded for these crossing wave systems, as discussed below.

Figs. 6a, d, and g show that the amplitude of the spatial troughs either side of the main crests (at  $t_{\text{focus}}$ ) tends to decrease with increased  $\Delta\theta$ . For  $\Delta\theta = 120^\circ$  and  $\Delta\theta = 60^\circ$ , the surface elevation along the observation direction  $\theta^*$  is almost entirely positive, and hence the definitions of characteristic wavelength based on zero crossing are challenging to apply, and the resulting steepness values potentially misleading. The local steepnesses of the crests shown in Figs. 6c, f, and i are comparable for all  $\Delta\theta$  values. However, owing to the actual zero-crossing locations, the crest-front steepness parameter values ( $\varphi_s$ ) in Tab. 4 differ greatly. A value of  $\varphi_s = 8.25^\circ$  is measured for  $\Delta\theta = 60^\circ$ , whereas much larger values are found for the other crossing angles.

Assessing the measurements along  $y^*$  in Figs. 6a, d, and g, it is clear that the transverse profiles of the waves differ greatly between the three crossing angles. For  $\Delta\theta = 0^\circ$ , the profile along  $y^*$  (i.e.,  $\theta = \theta^* + \pi/2$ ) is very broad and remains positive (non zero-crossing), indicating that there is a clear wave propagation direction (namely,  $x^*$ ) and that  $y^*$  is aligned with the crest of the wave. For  $\Delta\theta = 60^\circ$  and  $120^\circ$ , the profile along  $y^*$  becomes negative (zero-crossing) and is associated with comparable ( $\Delta\theta = 60^\circ$ ) or greater ( $\Delta\theta = 120^\circ$ ) local steepness to the steepness observed along  $x^*$ . This further highlights the extreme spatial localisation of large wave events associated with highly directionally spread and crossing sea states, and the difficulty in defining representative geometric

parameters.

Figs. 6b, e, and h show the wavelength  $L_2$  as a function of the observation angle  $\theta$  at the time of focus (note that  $L_1(\theta) = L_2(\theta + \pi)$ ). This illustrates the wave's geometry in 3D. For  $\Delta\theta = 0^\circ$  in Fig. 6b, the geometry is as would be expected for a nonlinear, weakly directionally spread wave: we observe front-to-rear asymmetry [58, 59] when comparing  $L_1$  and  $L_2$  in Tab. 4, and the wave is long crested (i.e., there are no zero-crossings and hence no values of  $L_2$  for angles that are nearly perpendicular to the wave propagation direction). For the  $\Delta\theta = 60^\circ$  and  $\Delta\theta = 120^\circ$  cases (Figs. 6e and h, respectively), the geometric parameters are more complex. For both cases, the range of angles  $\theta$  for which zero-crossings allows for calculation of wavelengths  $L_2$  is larger than for  $\Delta\theta = 0^\circ$ . For  $\Delta\theta = 120^\circ$ , wavelengths  $L_2$  can be computed for nearly all angles, demonstrating that the surface elevation has an apparent trough in all directions.

### 3.3. Wave Kinematics

As directional spreading increases, so does the proportion of wave components that travel normal to a given mean direction. As a result, the formation of partial standing waves and the cancellation of horizontal fluid motion occurs. This effect of directional spreading is a basic feature of linear wave theory; it is well documented and commonly accounted for in engineering practise using velocity reduction factors for the calculation of kinematics and resulting wave loads in moderately spread conditions [60]. It is less well documented how kinematics change in highly directionally spread conditions and how this can affect wave breaking, alongside the loading of structures. Crossing conditions provide realistic scenarios for very highly directionally spread seas and are associated with greatly reduced horizontal fluid velocities. In MC19, it was hypothesised that this cancellation of horizontal fluid velocity may allow the formation of larger wave amplitudes before breaking occurs. Here, we use our numerical simulations to quantify how significantly crossing conditions affect wave kinematics and we subsequently discuss in §3.4 how this may affect the onset of wave breaking.

Fig. 7 shows vertical profiles of absolute horizontal (a) and vertical (b) velocity components at the location of the crest of the waves immediately prior to breaking ( $t = 23.6$  s) for the three directional conditions simulated. The solid lines in (a) and (b) show the velocity reduction as a

percentage of the largest horizontal and vertical velocities, respectively (i.e., of the following-sea case with  $\Delta\theta = 0^\circ$  in (a) and of the crossing case with  $\Delta\theta = 120^\circ$  in (b)). As the crossing angle is increased, the horizontal velocities and vertical velocities decrease and increase, respectively. This may explain the change in breaking behaviour and the jet formation observed in Fig. 4. For  $\Delta\theta = 60$  and  $120^\circ$ , the reduction of horizontal velocity is approximately 20% and 50%, respectively.

### 3.4. Wave Breaking

Our simulations qualitatively confirm that wave breaking behaviour is significantly different in crossing-sea than in following-sea conditions (cf. Fig. 4) and that this fundamentally different behaviour may allow for the creation of steeper waves, as hypothesized in MC19. In the following section, we use the additional insight that may be gained from high-fidelity numerical simulations to gain a deeper understanding of changes to wave breaking behaviour that occur as directional spreading is increased.

#### 3.4.1. Wave breaking behaviour

Fig. 8 superimposes simulated free surfaces of the three breaking waves we have examined ( $\Delta\theta = 0^\circ, 60^\circ, 120^\circ$ ). As the crossing angle  $\Delta\theta$  increases, overturning horizontal breaking motion is reduced. In addition to this, the local steepness of the free surface and the localisation of the breaking crest increase with increasing crossing angle. The large crest also persists for a shorter duration. This localisation may result in reduced dissipation owing to breaking. Our results also confirm that this change in breaking may support larger crest heights for larger crossing angles (Tab. 3).

#### 3.4.2. Crest velocity

Crest velocity features in various definitions of breaking [38] and is intrinsically linked to our understanding of wave breaking. Put simply, wave breaking occurs when the fluid within the crest of a wave travels faster than crest of the wave itself. More formally, so-called kinematic wave breaking criteria can be defined, in which the onset of breaking is predicted using the ratio of fluid to crest velocity [39]. Crest velocity is also used as a normalisation parameter for so-called

dynamical wave breaking criteria, which examine the ratio of energy flux to energy density at the wave crest [42].

In directionally spread sea states, extreme waves may form as a result of the directional focusing of many different wave components. When waves from opposing directions combine, standing waves form. Therefore, depending on the degree of spreading of a given sea state, extreme waves may form as partial standing waves. Crossing sea states in particular present a realistic scenario for creation of wave components that travel at large angles to each other and form partial standing waves. Such waves can also be created by bathymetric focusing and reflection [61]. In the case of a purely standing wave, crests do not travel, and the crest velocity is ill defined. As a result, the applicability of wave breaking criteria based on crest velocity for highly directionally spread waves may be problematic.

Generally, it is not possible to measure crest velocity without high-resolution spatio-temporal measurements of surface elevation. If the necessary data is available, measuring crest velocity for waves which are narrow banded in both frequency and direction is relatively trivial. For 2D or ‘following’ waves, crests propagate in a single mean direction (cf. Fig. 9a and e). In complex crossing conditions, an (instantaneous) crest direction must be estimated one way or another. If a wave forms as a result of many different dispersively focusing components, the appropriate location of its crest can be difficult to identify (see also [38]), particularly immediately prior to breaking where large asymmetry and sharp changes in surface elevation can be observed (Fig. 9a).

We define a wave crest as a maximum of the free surface between consecutive zero up- and down-crossings. At times when crests are relatively flat (illustrated in 2D in Fig. 9a), the position of the maximum can jump rapidly in time and cause large spikes in estimated crest velocity and direction. To attempt to reduce this sensitivity, we approximate the position of the crest by taking the mean of the top 1% of particles at the free surface (in the region  $-2 < x < 2$  m and  $-2 < y < 2$  m) at each time step, shown as the red-shaded areas in Figs. 9e, f, and g. We note that, alternatively, near breaking, the crest of a wave may be defined as the sharp change in slope at the front of the wave, which is not necessarily the highest point. The grey markers in Figs. 9b,c and d show the crest speed calculated using the positions of the single highest points, and the red markers show the speed obtained from the mean of the (1%) highest points. Using the mean position of the

highest points somewhat smooths the resulting speed, but some large fluctuations still remain. In Fig. 9, panel a shows the crests at different times for the following-sea case in 1D. Panels e-g show the time-evolution of the crest locations  $\mathbf{x}_p = (x_p(t), y_p(t))$  in 2D for  $\Delta\theta = 0, 60, \text{ and } 120^\circ$ , respectively. Crest velocities are calculated using 4th-order central differences of crest position.

Figs. 9b-d show the crest speeds measured as a function of time for the three experiments. In all three cases, the wave crests travel in a reasonably constant direction during formation of the extreme crests, as evident from Figs. 9e-g. In the crossing cases, as the wave crest forms, it travels in an oblique direction to the two combining wave groups, namely at  $\theta = \theta^* \approx 35^\circ$  and  $\theta = \theta^* \approx 50^\circ$  for  $\Delta\theta = 60^\circ$  and  $120^\circ$ , respectively. Although crossing conditions create a partial standing wave, the crest velocity calculated by tracking the maxima of surface elevation suggests that crest speed is actually greater than for following-sea conditions, albeit in an oblique direction to the crossing components. The estimated crest speeds at  $t = 24$  s (time of focus) are 1.98, 2.48, and  $2.88 \text{ ms}^{-1}$ , for  $\Delta\theta = 0^\circ, 60^\circ$ , and  $120^\circ$ , respectively. Although this result may seem counter intuitive, this may be explained by considering the linear phase speed of two equal-amplitude crossing waves:  $\eta = a \cos(kx - \omega t) + a \cos(kx \cos \Delta\theta + ky \sin \Delta\theta - \omega t)$ . In this case, the phase speeds is given by  $|c_p| = c \sqrt{2/(1 + \cos \Delta\theta)}$ , which increases with crossing angle  $\Delta\theta$ , reaching a singularity at  $\Delta\theta = 180^\circ$  as the waves become purely standing (note  $c_p \equiv \omega k/|k|^2$ ,  $c = \omega/k$ ,  $k = |k|$ ).

### 3.4.3. Wave breaking criteria and prediction

Our results show that a large degree of directional spreading (in the form of crossing) has a strong effect on maximum steepness, fluid velocity, and crest velocity. The combined effect of these properties determine when the onset of wave breaking occurs. We have observed in §3.2 that wave steepness  $2\pi\eta_c/L$  varies significantly depending on how wavelength  $L$  is calculated, and does not reflect local crest steepness. Particularly in the case of highly directionally spread waves, where characteristic wavelength is poorly defined, geometric criteria such as steepness do not function as robust parameters for predicting the onset of wave breaking.

In general, kinematic and dynamic criteria have been shown to provide more robust indications of when breaking may occur [38]. Both types of criteria rely upon knowledge of fluid and crest velocities, which rules them out for predictive use. These criteria may still be used to detect when

wave breaking has occurred during simulations that are capable of modelling breaking, such as  
 ours. Barthelemy et al. [42] defined a dynamic criterion  $B = |F|/(E|c|)$  based on the ratio of  
 energy flux  $F$  to energy density  $E$ , which is normalised by crest speed  $|c|$ . At the surface,  $|F|/E$   
 may be expressed as the total fluid velocity  $|u|$  (at the surface), resulting in the criterion  $B = |\mathbf{u}|/|c|$   
 [42]. In following-sea conditions, [42] suggest that  $B$  and  $B_x = u_x/c_x$  are equivalent and found that,  
 when  $B_x$  exceeds a value of 0.86, breaking will occur based on the experiments and simulations  
 they examined. The same value of  $u_x/c_x$  was obtained in [62] in an earlier study of periodic waves.  
 This criterion has also been demonstrated to be effective for predicting the onset of breaking in  
 shallow water using numerical simulations [43].

In the simulations and experiments presented herein, it is clear that breaking has occurred  
 (cf. Figs. 4 and 8). However, the crossing waves we simulate have reduced fluid velocities and  
 increased crest velocities, which will both reduce the value of  $B$  when compared to the following-  
 sea case. In the first two simulations ( $\Delta\theta = 0, 60^\circ$ ), values of the parameter  $B$  exceed 0.86 at  
 various times. When  $\Delta\theta = 120^\circ$ , a very small region of the surface approaches this limit at  $t = 24.3$   
 s ( $B = 0.8582$ ). In Fig. 10, panels a, b, and c, show the first instance in time at which  $B \geq 0.86$ .  
 If we also consider vertical or double valued-free surface as an indication of breaking [42], we  
 may establish if these values have occurred after the onset of wave breaking. Panels d to f show  
 the vertical component  $n_z$  of the unit normal vector of the simulated free surface;  $-1 < n_z \leq 0$   
 represents a vertical or overturning free surface. Panels d and e illustrate that at these instances  
 in time the surface is not yet vertical, and hence  $B$  may provide a robust indication that breaking  
 is about to occur. However, in panel f, a portion of the surface has already started to overturn. In  
 panels g-i, we plot the maximum value of  $B$  observed in the region  $-2 < x < 2$  m and  $-2 < y < 2$   
 m and the percentage of the surface that has a slope  $n_z < 0$  as a function of time for each crossing  
 angle. In all three cases, the values of  $B$  vary significantly in time, only becoming consistently  
 greater than 0.86 once a considerable portion of the free surface has become overturning. This  
 variability is a direct result of fluctuations in crest velocity; the blue open circles show the results  
 of calculating  $B$  using constant velocities calculated at  $t = 24$  s.

Our simulated results illustrate that the criterion  $B > 0.86$  shows promise as a means of pre-  
 dicting the onset of wave breaking in moderately directionally spread scenarios. For the most

directionally spread case, the criterion may fail to predict the onset of breaking. In performing our analysis, it is clear that the crest speed, which is a prerequisite parameter for the evaluation of the breaking criterion, is not necessarily well defined. To fully understand the robustness of the parameter  $B$  a more comprehensive study of both breaking and non breaking highly directionally spread waves is necessary.

## 4. Conclusions

We have performed SPH simulations of highly directionally spread, breaking waves in the form of a case study of the Draupner wave [1]. Simulations were carried using a numerical model of the FloWave Ocean Energy Research Facility wave tank [37]. The numerical model was used to reproduce experiments carried out by MC19 [36] in the same facility, allowing for direct validation of the SPH model. In the experiments and simulations, waves were created using the same wavemaker displacements. A total of 127 million particles were required to achieve a satisfactory level of convergence and agreement between the experiments and simulations when simulating the 25 m diameter tank. This corresponds to a particle distance of 2 cm, approximately 500 particles per wavelength, or 37 particles over the maximum wave height.

In doing so, we have shown that the SPH method is an effective tool for high-fidelity modelling of very steep, highly directionally spread breaking waves. In particular, this particle-based method is a very suitable method for numerically replicating a physical wave tank, including its wavemakers. This method also allows wave breaking processes to be modelled, and shows good promise for furthering understanding of wave breaking and extreme waves.

In the three experiments simulated, the numerical model reproduced time-series measurements recorded during physical experiments well, achieving  $r^2$  values of approximately 0.94. At the gauges downstream of the maximum wave height and violent breaking, good agreement between experiments and simulations is maintained. Qualitative observations made using still images showed that wave breaking behaviour is reproduced well by the model. Some small-scale features, such as a spray and white water, were less well captured. It is likely that a particle spacing of less than 2 cm may be required to reproduce features on this scale, which may also be affected by phenomena not explicitly modeled in our simulations, such as surface tension and the presence

of air. One of the main observations in MC19 was that the form of wave breaking changed from plunging breaking to an upward jet, as the crossing angle was increased. Our simulations confirm this.

Our highly spatially resolved simulations allow for the direct measurement of various aspects of wave geometry, which forms the basis of commonly used wave breaking criteria. We find that wavelengths measured spatially can be vastly different than those approximated from time-series measurements, an approximation commonly made to implement geometric wave breaking criteria. In the following-sea case ( $\Delta\theta = 0^\circ$ ), where there is little ambiguity how to define wavelength, temporal approximation leads to an error of around 20% (in wavelength) and fails to capture the large horizontal and vertical asymmetry observed. The same is true for the crossing cases ( $\Delta\theta = 60^\circ$ ,  $\Delta\theta = 120^\circ$ ) when considering properties calculated along the instantaneous crest direction  $x^*$ . Steepness calculated as  $2\pi\eta_c/L$  is also shown to bear little correlation to actual crest steepness. These results highlight two main outcomes. First, time-domain approximations of geometric properties perform poorly in the highly spread and steep conditions we examine. Second, a systematic and comprehensive study breaking and non breaking waves is required to define and understand the relevance of geometric measures for highly directional spread waves.

Our simulations confirm that, as we increase crossing angle, a partial standing wave forms and horizontal and vertical velocities reduce by approx 20%, and 50% for  $\Delta\theta = 60^\circ$  and  $120^\circ$ , respectively. This measured reduction in horizontal fluid velocity helps to explain the changes in breaking behaviour observed in MC19. Partial standing wave formation that occurs in highly spread conditions make estimating crest velocity challenging, and, as a result, kinematic and dynamical breaking criteria become difficult to evaluate robustly. Crests appear to travel in oblique directions and at greater speeds than for a following wave. Combined with reductions in fluid velocity, this may allow for the creation of steeper waves prior to breaking. Despite the challenges in estimating the value of  $B$  in [42]’s breaking criterion, their threshold value of  $B = 0.86$  is exceeded or met in all our simulations. We believe a more comprehensive study of breaking and non-breaking waves is required to demonstrate the effectiveness of dynamical (i.e.  $B$ ) and kinematic criteria for highly spread waves.

## Acknowledgements

We would like to thank Dr Donald Noble at the University of Edinburgh for taking the photographs presented in Fig. 4. This work was partly financed by JSPS Overseas Challenge Program for Young Researches and JSPS KAKENHI Grant Numbers 20K22396 and 20H02369. TvdB acknowledges a Royal Academy of Engineering Research Fellowship. SD acknowledges a Dame Kathleen Ollerenshaw Fellowship. We acknowledge EPSRC grant EP/I02932X/1 for funding the construction of FloWave.

## References

- [1] S. Haver, A possible freak wave event measured at the Draupner jacket January 1 1995, in: Rogue Waves Workshop, Brest, France, 2004, pp. 1–8.
- [2] A. K. Magnusson, M. A. Donelan, The Andrea wave characteristics of a measured North Sea rogue wave, *Journal of Offshore Mechanics and Arctic Engineering* 135 (2013) 031108.
- [3] J. D. Flanagan, F. Dias, E. Terray, B. Strong, J. Dudley, Extreme water waves off the west coast of Ireland: Analysis of ADCP measurements, in: The 26th International Ocean and Polar Engineering Conference, 2016, pp. ISOPE–I–16–589.
- [4] C. Guedes Soares, E. Bitner-Gregersen, P. Antão, Analysis of the frequency of ship accidents under severe north atlantic weather conditions, in: Proceedings of the Conference on Design and Operation for Abnormal Conditions II (RINA), 2001, pp. 221–230.
- [5] A. Toffoli, J. M. Lefèvre, E. Bitner-Gregersen, J. Monbaliu, Towards the identification of warning criteria: Analysis of a ship accident database, *Applied Ocean Research* 27 (6) (2005) 281 – 291.
- [6] H. Tamura, T. Waseda, Y. Miyazawa, Freakish sea state and swell-windsea coupling: Numerical study of the Suwa-Marui incident, *Geophysical Research Letters* 36 (1) (2009).
- [7] L. Cavaleri, L. Bertotti, L. Torrisi, E. Bitner-Gregersen, M. Serio, M. Onorato, Rogue waves in crossing seas: The Louis Majesty accident, *J. Geophys. Res.-Oceans* 117 (C11) (2012).
- [8] K. Trulsen, J. C. Nieto Borge, O. Gramstad, L. Aouf, J. Lefèvre, Crossing sea state and rogue wave probability during the prestige accident, *Journal of Geophysical Research: Oceans* 120 (10) (2015) 7113–7136.
- [9] Z. Z. Zhang, X.-M. Li, Global ship accidents and ocean swell-related sea states, *Natural Hazards and Earth System Sciences* 17 (11) (2017) 2041–2051.
- [10] K. B. Dysthe, H. E. K. P. Müller, Oceanic rogue waves, *Annu. Rev. Fluid Mech.* 40 (2008) 287–310.
- [11] C. Kharif, E. Pelinovsky, Physical mechanisms of the rogue wave phenomenon, *Eur. J. Mech. B-Fluid.* 22 (2003) 603–634.

- 552 [12] T. A. A. Adcock, P. H. Taylor, The physics of anomalous ('rogue') ocean waves, *Rep. Prog. Phys.* 465 (2014)  
553 3361–3381.
- 554 [13] J. M. Dudley, G. Genty, A. Mussot, Chabchoub, F. Dias, Rogue waves and analogies in optics and oceanography,  
555 *Nature Reviews Physics* 1 (11) (2019) 675–689.
- 556 [14] E. Bitner-Gregersen, L. Fernández, J. Lefèvre, J. Monbaliu, A. Toffoli, The north sea andrea storm and numerical  
557 simulations, *Natural Hazards and Earth System Sciences* 14 (6) (2014) 1407–1415.
- 558 [15] F. Fedele, J. Brennan, S. P. De León, J. Dudley, F. Dias, Real world ocean rogue waves explained without the  
559 modulational instability, *Scientific Reports* 6 (2016) 27715.
- 560 [16] A. Alberello, A. Chabchoub, J. P. Monty, F. Nelli, J. H. Lee, J. Elsnab, A. Toffoli, An experimental comparison  
561 of velocities underneath focussed breaking waves, *Ocean Engineering* 155 (2018) 201–210.
- 562 [17] D. Fuster, G. Agbaglah, C. Josserand, S. Popinet, S. Zaleski, Numerical simulation of droplets, bubbles and  
563 waves: state of the art, *Fluid dynamics research* 41 (6) (2009) 065001.
- 564 [18] L. Deike, W. K. Melville, S. Popinet, Air entrainment and bubble statistics in breaking waves, *Journal of Fluid*  
565 *Mechanics* 801 (2016) 91–129.
- 566 [19] F. De Vita, R. Verzicco, A. Iafrati, Breaking of modulated wave groups: kinematics and energy dissipation  
567 processes, *Journal of fluid mechanics* 855 (2018) 267–298.
- 568 [20] E. Dinesh Kumar, S. Sannasiraj, V. Sundar, Phase field lattice boltzmann model for air-water two phase flows,  
569 *Physics of Fluids* 31 (7) (2019) 072103.
- 570 [21] F. Yamada, K. Takikawa, et al., Improving the accuracy of free-surface recognition and conservation of mass for  
571 the volume of fluid method, in: *The Ninth International Offshore and Polar Engineering Conference*, International  
572 Society of Offshore and Polar Engineers, 1999.
- 573 [22] J. Monaghan, Simulating free surface flows with SPH, *Journal of Computational Physics* 110 (2) (1994) 399 –  
574 406.
- 575 [23] D. Molteni, A. Colagrossi, A simple procedure to improve the pressure evaluation in hydrodynamic context  
576 using the SPH, *Computer Physics Communications* 180 (6) (2009) 861–872.
- 577 [24] G. Fourtakas, J. M. Dominguez, R. Vacondio, B. D. Rogers, Local uniform stencil (LUST) boundary condition  
578 for arbitrary 3-D boundaries in parallel smoothed particle hydrodynamics (SPH) models, *Computers & Fluids*  
579 190 (2019) 346–361.
- 580 [25] S. J. Lind, R. Xu, P. K. Stansby, B. D. Rogers, Incompressible smoothed particle hydrodynamics for free-surface  
581 flows: A generalised diffusion-based algorithm for stability and validations for impulsive flows and propagating  
582 waves, *Journal of Computational Physics* 231 (4) (2012) 1499–1523.
- 583 [26] X. Rui, P. K. Stansby, D. Laurence, Accuracy and stability in incompressible sph (isph) based on the projection  
584 method and a new approach, *Journal of computational Physics* 228 (18) (2009) 6703–6725.
- 585 [27] J. J. Monaghan, A. Kos, Solitary waves on a Cretan Beach, *Journal of Waterway, Port, Coastal, and Ocean*

Engineering 125 (3) (1999) 145–155.

- [28] R. J. Farahani, R. A. Dalrymple, Three-dimensional reversed horseshoe vortex structures under broken solitary waves, *Coastal Engineering* 91 (2014) 261 – 279.
- [29] D. D. Meringolo, Y. Liu, X. Wang, A. Colagrossi, Energy balance during generation, propagation and absorption of gravity waves through the -LES-SPH model, *Coastal Engineering* 140 (2018) 355 – 370.
- [30] R. J. Lowe, M. L. Buckley, C. Altomare, D. P. Rijnsdorp, Y. Yao, T. Suzuki, J. D. Bricker, Numerical simulations of surf zone wave dynamics using smoothed particle hydrodynamics, *Ocean Modelling* 144 (2019) 101481.
- [31] M. Antuono, A. Colagrossi, S. Marrone, C. Lugni, Propagation of gravity waves through an sph scheme with numerical diffusive terms, *Computer Physics Communications* 182 (4) (2011) 866–877.
- [32] A. Colagrossi, A meshless lagrangian method for free-surface and interface flows with fragmentation, Ph.D. thesis, Universita di Roma, La Sapienza (2005).
- [33] R. A. Dalrymple, B. D. Rogers, Numerical modeling of water waves with the sph method, *Coastal Engineering* 53 (2) (2006) 141 – 147.
- [34] M. Dao, H. Xu, E. Chan, P. Tkalich, Numerical modelling of extreme waves by smoothed particle hydrodynamics, *Natural Hazards and Earth System Sciences* 11 (2) (2011) 419.
- [35] A. D. Chow, D. D. Rogers, S. J. Lind, P. K. Stansby, Numerical wave basin using incompressible smoothed particle hydrodynamics (isph) on a single gpu with vertical cylinder test cases, *Computers & Fluids* 179 (2019) 543–562.
- [36] M. L. McAllister, S. Draycott, T. A. A. Adcock, P. H. Taylor, T. S. van den Bremer, Laboratory recreation of the Draupner wave and the role of breaking in crossing seas, *J. Fluid Mech.* 860 (2019) 767–786.
- [37] T. Kanehira, H. Mutsuda, Y. Doi, N. Taniguchi, S. Draycott, M. I. D, Development and experimental validation of a multidirectional circular wave basin using smoothed particle hydrodynamics, *Coastal Engineering Journal* 61 (1) (2019) 109–120.
- [38] M. Perlin, W. Choi, Z. Tian, Breaking waves in deep and intermediate waters, *Annu. Rev. Fluid Mech.* 45 (2013) 115–145.
- [39] P. Stansell, C. MacFarlane, Experimental investigation of wave breaking criteria based on wave phase speeds, *J. Pphys Oceanog.* 32 (5) (2002) 1269–1283.
- [40] A. Saket, W. L. Peirson, M. L. Banner, X. Barthelemy, M. J. Allis, On the threshold for wave breaking of two-dimensional deep water wave groups in the absence and presence of wind, *J. Fluid Mech.* 811 (2017) 642–658.
- [41] A. Saket, W. L. Peirson, M. L. Banner, M. J. Allis, On the influence of wave breaking on the height limits of two-dimensional wave groups propagating in uniform intermediate depth water, *Coastal Engineering* 133 (2017) 159–165.
- [42] X. Barthelemy, M. L. Banner, W. L. Peirson, F. Fedele, M. Allis, F. Dias, On a unified breaking onset threshold for gravity waves in deep and intermediate depth water, *J. Fluid Mech.* (2018).

- [43] M. Derakhti, J. T. Kirby, M. L. Banner, S. T. Grilli, J. Thomson, A unified breaking onset criterion for surface gravity water waves in arbitrary depth (2019) 1–31.  
URL <http://arxiv.org/abs/1911.06896>
- [44] A. V. Babanin, T. Waseda, T. Kinoshita, A. Toffoli, Wave breaking in directional fields, *J. Phys. Oceanogr.* 41 (1) (2011) 145–156.
- [45] A. Crespo, J. Domínguez, B. Rogers, M. Gómez-Gesteira, S. Longshaw, R. Canelas, R. Vacondio, A. Barreiro, O. García-Feal, Dualsphysics: Open-source parallel CFD solver based on smoothed particle hydrodynamics (sph), *Computer Physics Communications* 187 (2015) 204 – 216.
- [46] T. Kanehira, H. Mutsuda, S. Draycott, N. Taniguchi, T. Nakashima, Y. Doi, D. M. Ingram, Numerical re-creation of multi-directional waves in a circular basin using a particle based method, *Ocean Engineering* 209 (2020) 107446.
- [47] R. A. Gingold, J. J. Monaghan, Smoothed particle hydrodynamics: theory and application to non-spherical stars, *Monthly Notices of the Royal Astronomical Society* 181 (3) (1977) 375–389.
- [48] H. Wendland, Piecewise polynomial, positive definite and compactly supported radial functions of minimal degree, *Advances in Computational Mathematics* 4 (1) (1995) 389–396.
- [49] E. Y. M. Lo, S. Shao, Simulation of near-shore solitary wave mechanics by an incompressible sph method, *Applied Ocean Research* 24 (5) (2002) 275 – 286.
- [50] H. Gotoh, Sub-particle-scale turbulence model for the mps method-lagrangian flow model for hydraulic engineering, *Computational Fluid Dynamics Journal* (2001) 339–347.
- [51] J. J. Monaghan, Smoothed particle hydrodynamics, *Annual Review of Astronomy and Astrophysics* 30 (1) (1992) 543–574.
- [52] D. Ingram, R. Wallace, A. Robinson, I. Bryden, The design and commissioning of the first, circular, combined current and wave test basin, in: *OCEANS 2014 - TAIPEI*, 2014, pp. 1–7.
- [53] A. J. C. Crespo, M. Gómez-Gesteira, R. A. Dalrymple, Boundary conditions generated by dynamic particles in SPH methods, *Computers, Materials and Continua* 5 (2007) 173–184.
- [54] T. A. A. Adcock, P. H. Taylor, S. Yan, Q. W. Ma, P. A. E. M. Janssen, Did the Draupner wave occur in a crossing sea?, *Proc. R. Soc. A* 467 (2011) 3004–3021.
- [55] C. Altomare, J. M. Domínguez, A. J. C. Crespo, J. González-Cao, T. Suzuki, M. Gómez-Gesteira, P. A. Troch, Long-crested wave generation and absorption for sph-based dualsphysics model, *Coastal Engineering* 127 (2017) 37–54.
- [56] A. Yao, C. H. Wu, Spatial and temporal characteristics of transient extreme wave profiles on depth-varying currents, *J. Eng. Mech.* 132 (2006) 1015–1025.
- [57] C. C. Craciunescu, M. Christou, On the calculation of wavenumber from measured time traces, *Applied Ocean Research* 98 (2020) 102115.

- 654 [58] T. A. A. Adcock, P. H. Taylor, S. Draper, Nonlinear dynamics of wave-groups in random seas: unexpected walls  
655 of water in the open ocean, *Proc. Roy. Soc. A* 471 (2184) (2015) 20150660.
- 656 [59] D. Barratt, H. B. Bingham, P. H. Taylor, T. S. van Den Bremer, T. A. A. Adcock, Rapid spectral evolution of  
657 steep surface wave groups with directional spreading, *J. Fluid Mech.* 907 (2021).
- 658 [60] R.-W. API, Recommended practice for planning, designing and constructing fixed offshore platforms—working  
659 stress design—, American Petroleum Institute, Washington Dc, (2000).
- 660 [61] L. Jiang, M. Perlin, W. W. Schultz, Period tripling and energy dissipation of breaking standing waves, *Journal*  
661 *of Fluid Mechanics* 369 (1998) 273–299.
- 662 [62] K. A. Chang, P. L. F. Liu, Velocity, acceleration and vorticity under a breaking wave, *Physics of Fluids* 10 (1)  
663 (1998) 327–329.

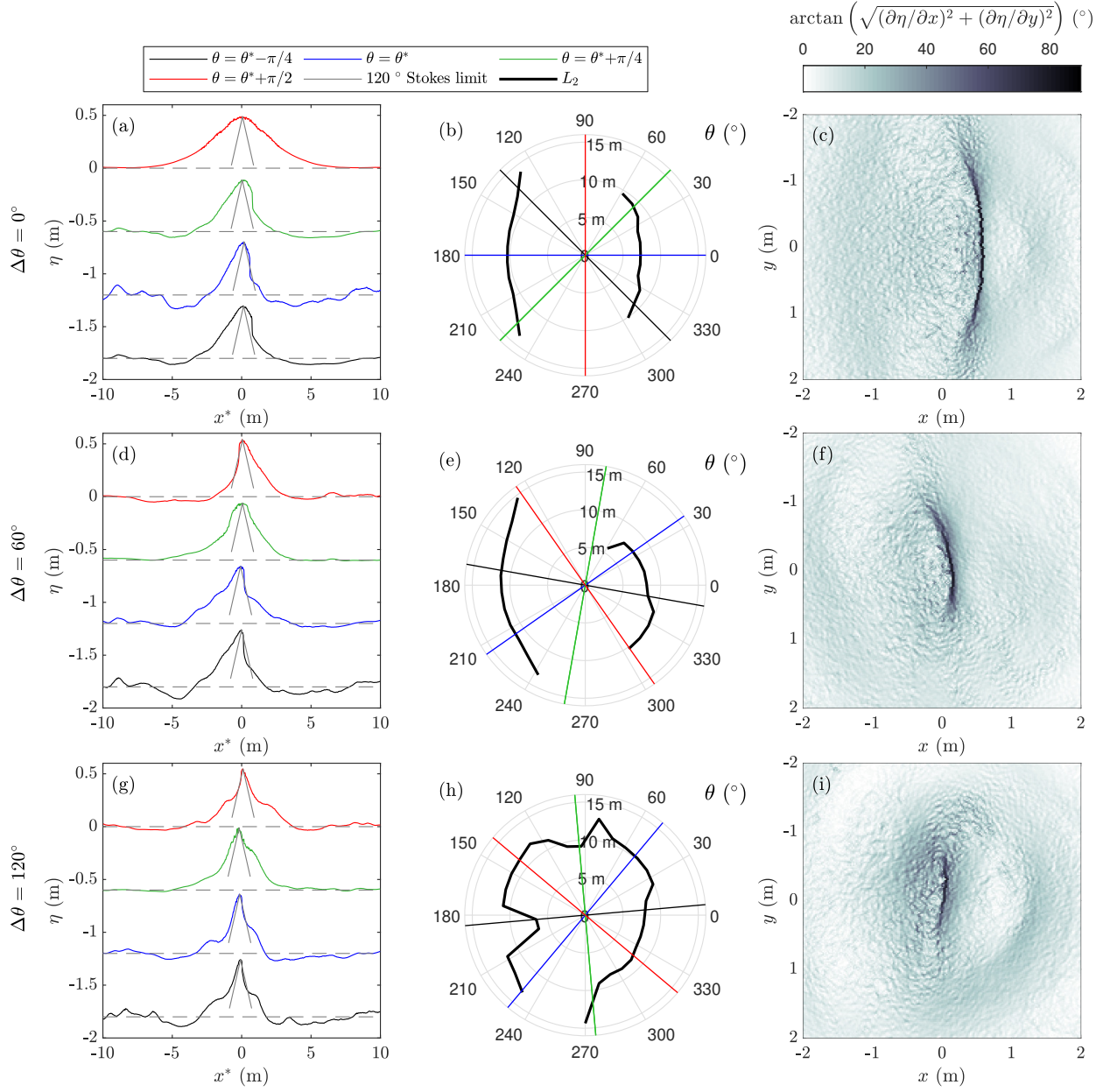


**Fig. 6** Spatial profiles of surface elevation in different observation directions (left column), wavelength  $L_2$  (thick black lines) as a function of observation angle  $\theta$  (middle column) and surface gradients (right column) for the three  $\Delta\theta$  values (rows). In panels a, d, and g, surface elevations are shown along four different observation directions, as defined in panels b, e, and h (black, blue, green and red lines).

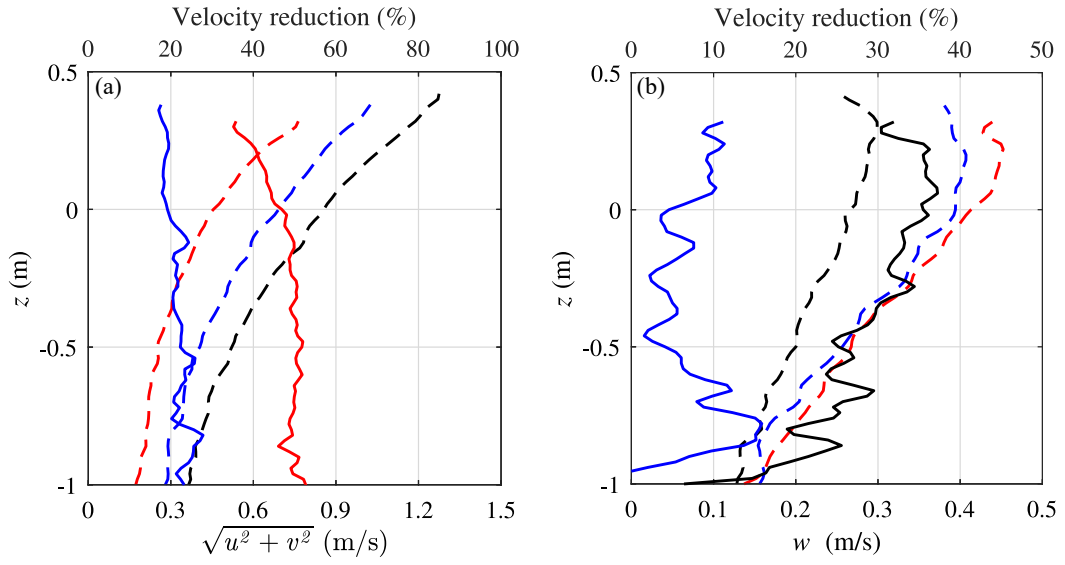


**Fig. 7** Vertical profiles of horizontal (a) and vertical (b) velocity measured at the location of the crest of the waves and time  $t = 23.6$  s for the three different crossing angles ( $\Delta\theta = 0^\circ$  in black,  $\Delta\theta = 60^\circ$  in blue, and  $\Delta\theta = 120^\circ$  in red), showing the dimensional velocity components as dashed lines on the bottom axes and the reduction in velocity as a percentage of the following-sea case ( $\Delta\theta = 0^\circ$ ) (a) and of the crossing case with  $\Delta\theta = 120^\circ$  (b) as solid lines on the top axes.

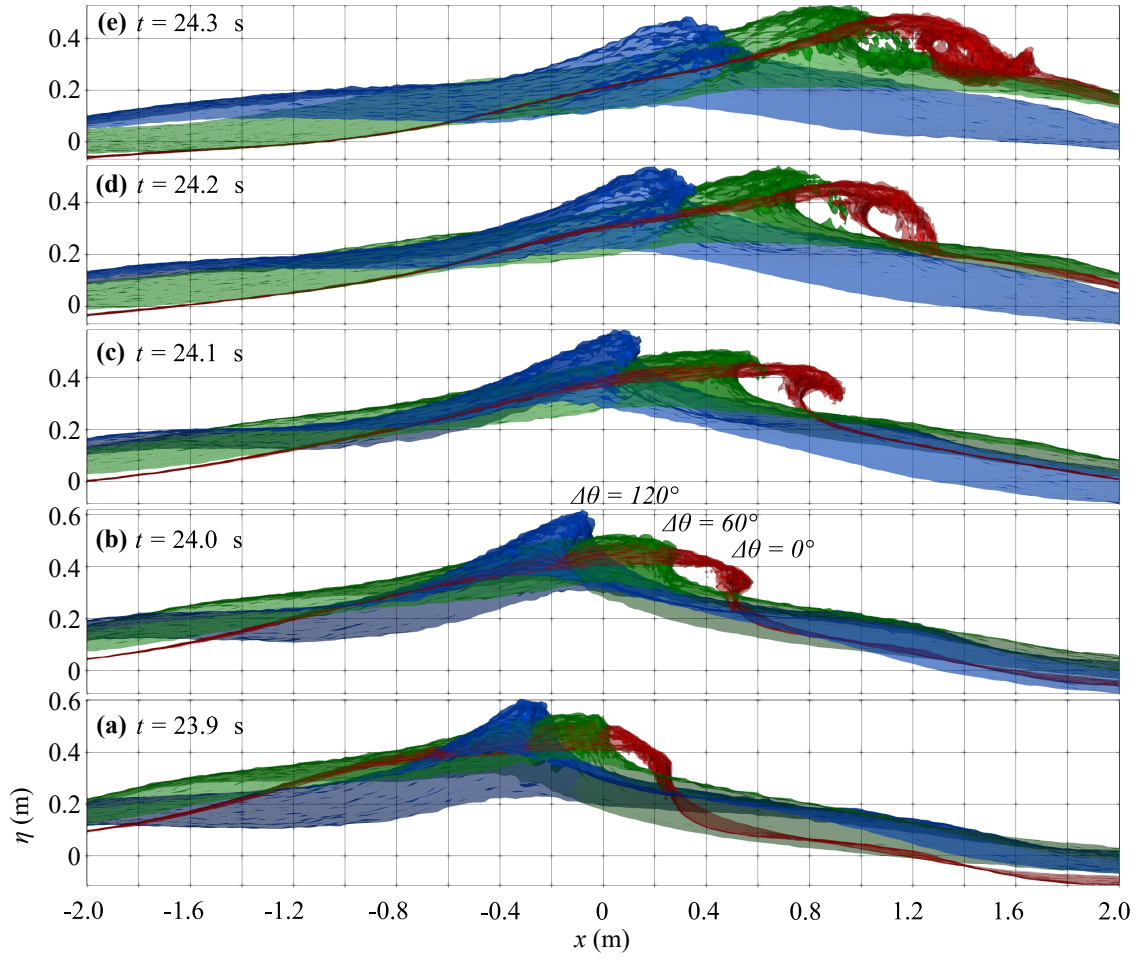


**Fig. 8** Comparison of the free surface elevation and breaking behaviour for the three crossing angles  $\Delta\theta = 0^\circ$  (red),  $60^\circ$  (green) and  $120^\circ$  (blue).

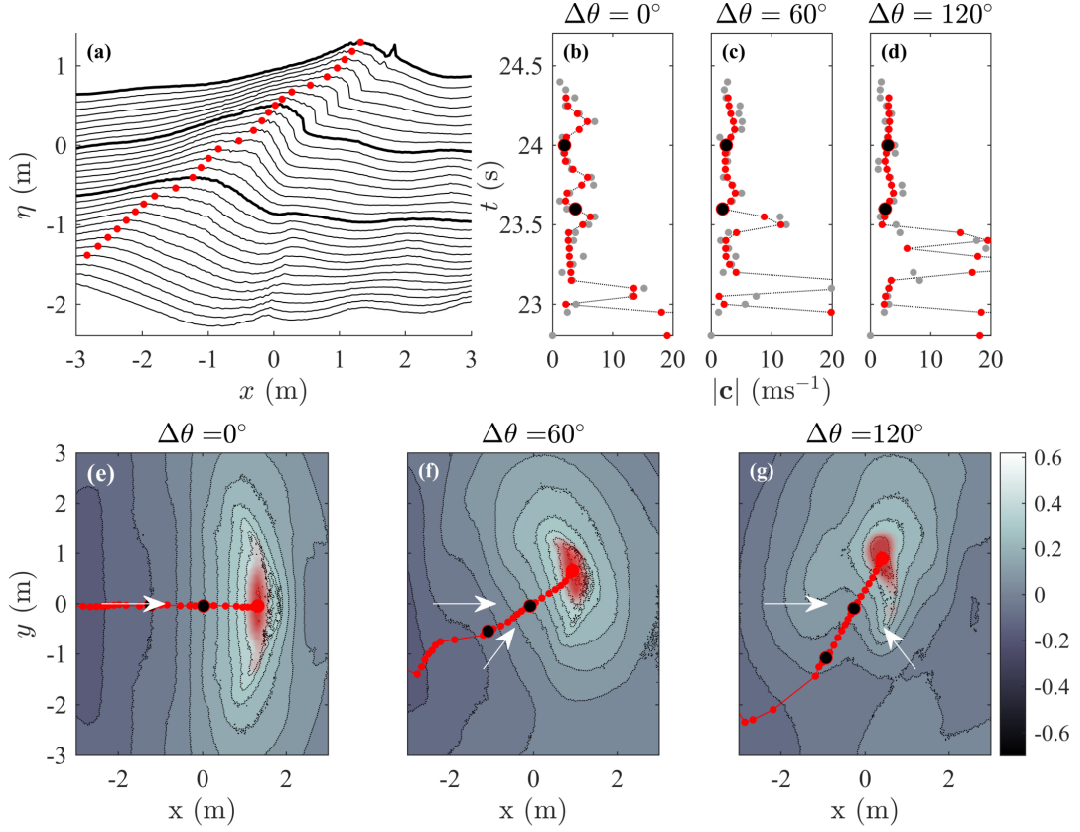


**Fig. 9** Illustration of crest identification and resulting instantaneous crest velocity: (a) crest identification in the  $x$ - direction only for  $\Delta\theta = 0^\circ$  with black lines showing surface elevation from  $t = 23$  to  $24.4$  s at  $0.05$  s intervals, thick lines corresponding to times  $t = 23.6, 24, 24.4$  s, and red dots showing identified crest locations at each time step; (b-d) corresponding crest speeds; (e-g) crest identification in the  $x$  and  $y$ -directions for  $\Delta\theta = 0^\circ, \Delta\theta = 60^\circ$  and  $120^\circ$ , respectively, with contours showing surface elevation at  $t = 24.4$  s, small red markers showing previous crest locations at  $0.05$  s intervals, black markers showing crest locations at  $t = 23.6, 24$  s, red-shaded area showing particles used to locate crest at  $t = 24.4$  s, and white arrows showing the directions of travel of the main and transverse waves.

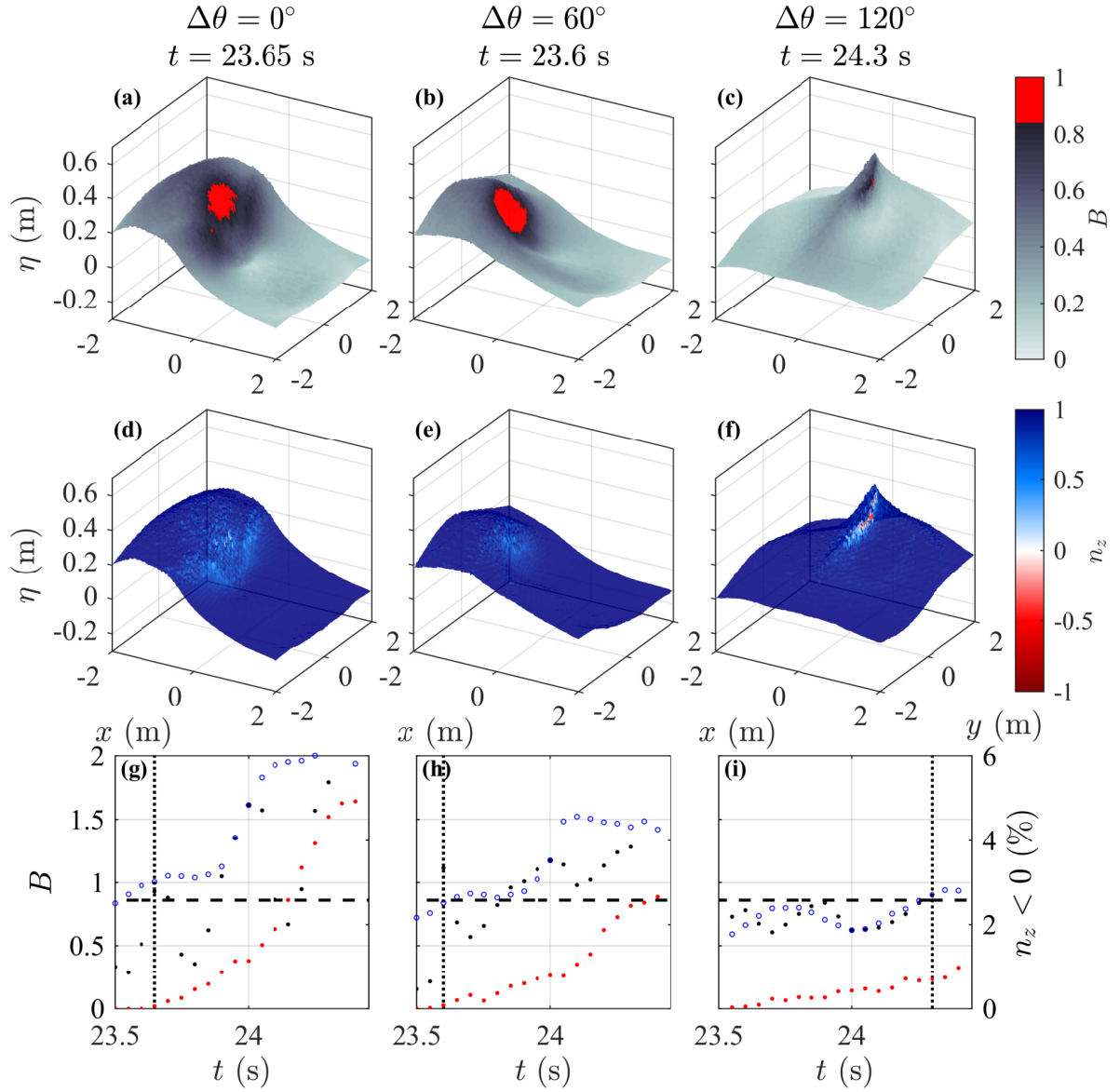


**Fig. 10** Breaking onset detection for  $\Delta\theta = 0^\circ$  (left column),  $60^\circ$  (middle column), and  $120^\circ$  (right column): (a-c) values of the parameter  $B$  plotted on the surface elevation  $\eta$ ; (d-f) values of the vertical component of surface normal vector  $n_z$  plotted on surface elevation  $\eta$ ; (g) to (f) black dots show maximum value of parameter  $B = |u|/|c|$  calculated using instantaneous crest velocity (see §3.4.2), blue open circles show the same calculation for constant crest velocity, and red dots show the percentage of the surface which is vertical or overturning ( $n_z < 0$ ) as a function of time, the horizontal dashed black line shows  $B = 0.86$ , and the vertical dotted black line shows the time at which  $B$  exceeds 0.86 for the first time, which corresponds to the panels above.